OPEN ACCESS

Materials Chemistry REPORT

Suppressing antiparallel dipole alignment: A molecular engineering strategy toward sem-organic UV NLO crystals

Guangsheng Xu,[1,2] Xue Bai,[1] Zhihua Yang,[1,2] Xueling Hou,[1,2] Jian Han,[1,2,*] and Shilie Pan[1,2,*]

*Correspondence: hanjian@ms.xjb.ac.cn (J.H.); slpan@ms.xjb.ac.cn (S.P.)

Received: November 28, 2025; Accepted: May 12, 2026; Published Online: May 12, 2026; https://doi.org/10.59717/j.xinn-mater.2026.100218

GRAPHICAL ABSTRACT

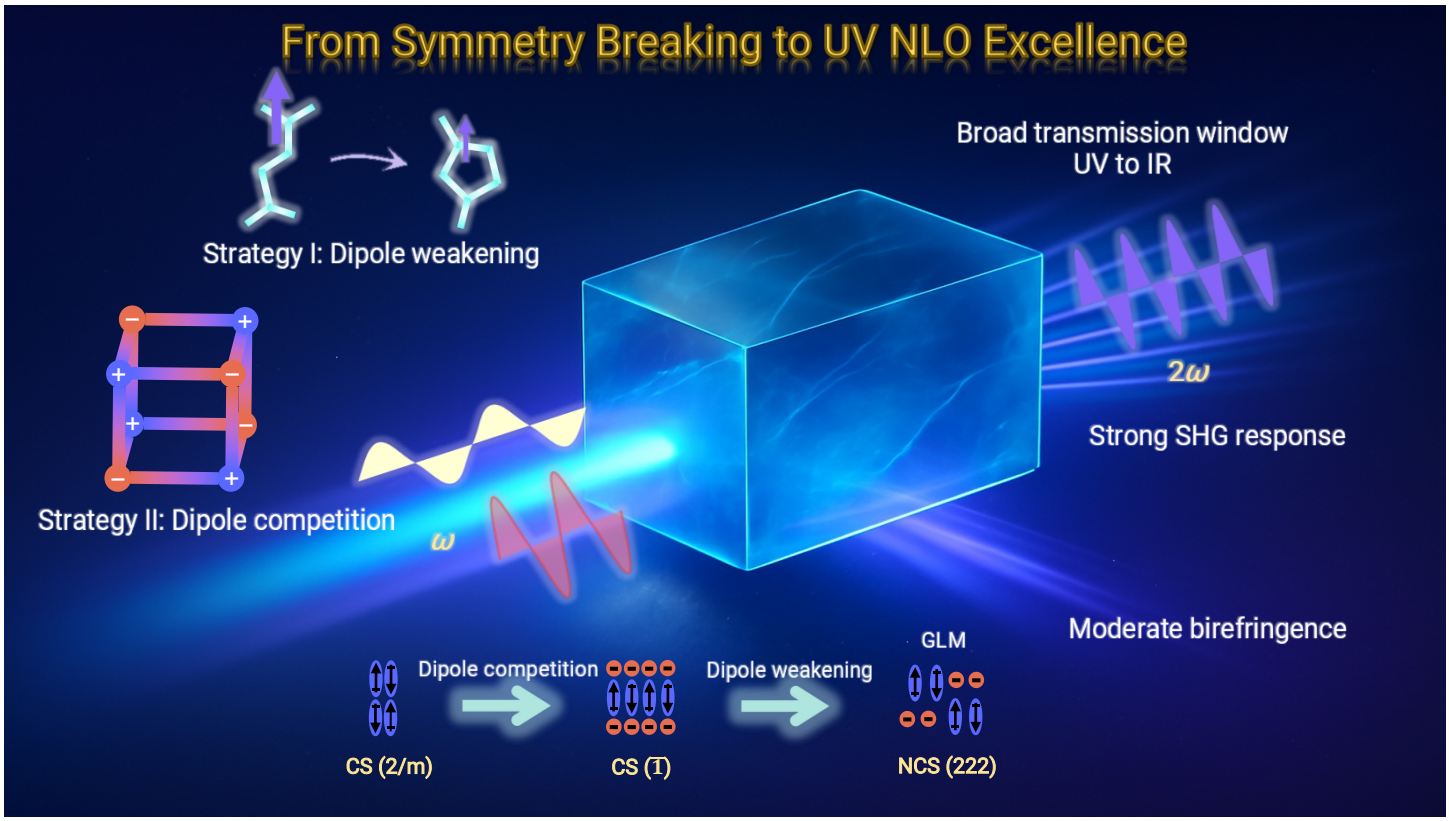

PUBLIC SUMMARY

- A dual molecular strategy to construct non-centrosymmetric semi-organic nonlinear optical crystals.
- Identification of a novel highly efficient nonlinear optical chromophore suitable for the ultraviolet region.
- $(C_3N_3OH_6)(CH_3SO_3)$, an outstanding nonlinear optical crystal, achieves thermal-induced symmetry breaking.

REPORT Materials Chemistry

www.the-innovation.org/the-innovation-materials

Suppressing antiparallel dipole alignment: A molecular engineering strategy toward sem-organic UV NLO crystals

Guangsheng Xu,[1,2] Xue Bai,[1] Zhihua Yang,[1,2] Xueling Hou,[1,2] Jian Han,[1,2,*] and Shilie Pan[1,2,*]

[1]Research Center for Crystal Materials; CAS Key Laboratory of Functional Materials and Devices for Special Environmental Conditions; Xinjiang Key Laboratory of Functional Crystal Materials, Xinjiang Technical Institute of Physics and Chemistry, Chinese Academy of Sciences, Urumqi 830011, China

[2]Center of Materials Science and Optoelectronics Engineering, University of Chinese Academy of Sciences, Beijing 100049, China

*Correspondence: hanjian@ms.xjb.ac.cn (J.H.); slpan@ms.xjb.ac.cn (S.P.)

Received: November 28, 2025; Accepted: May 12, 2026; Published Online: May 12, 2026; https://doi.org/10.59717/j.xinn-mater.2026.100218

Citation: Xu G., Bai X., Yang Z., et al. (2026). Suppressing antiparallel dipole alignment: A molecular engineering strategy toward sem-organic UV NLO crystals. *The Innovation Materials* **4**:100218.

Designing crystalline materials with exceptional nonlinear optical (NLO) performance for all-solid-state lasers is a challenging task. In covalent compounds, organic groups with large molecular dipole moments (μ) tend to form antiparallel dimers, leading to a high probability of crystallization in centrosymmetric (CS) structures. This study proposes a dual molecular engineering strategy, which involves reducing the ground-state dipole moment of functional molecules and introducing counterions for dipole competition, to guide self-assembly and optimize the performance of semi-organic crystals. Applied to the CS compound $(C_3N_3O_2H_8)(CH_3SO_3)\cdot H_2O$ (HGM), symmetry breaking occurs through thermally induced structural evolution. The resulting NLO material, $(C_3N_3OH_6)(CH_3SO_3)$ (GLM), exhibits exceptional solar-blind ultraviolet performance. It demonstrates advantages over the commercial semi-organic NLO crystal LAP in several key aspects, including superior thermal stability, a broader transmission range, a stronger second-harmonic response (2.0 × KDP), and a suitable birefringence (Δn = 0.078@546 nm). First-principles calculations reveal that the π-conjugated $(C_3N_3OH_6)^+$ cation governs its strong optical anisotropy and NLO response. This work establishes a new paradigm for designing high-performance semi-organic NLO crystals.

INTRODUCTION

Driven by the dual forces of technological innovation and the surging demand for modern equipment, all-solid-state direct-technology-based coherent lasers utilizing nonlinear optical (NLO) crystals have emerged as pivotal enabling technologies across multidisciplinary domains. These systems provide core solutions for cutting-edge applications, including optoelectronic data storage, optoelectronic information processing, precision micro-nano fabrication, biological microscopic imaging, and ultrafast spectroscopic analysis.[1-6] Notably, breakthrough applications in the ultraviolet (UV) spectral region have demonstrated remarkable prominence.[7-9] For inorganic materials, compounds such as KDP, BBO, LBO, KBBF, and ABF have been demonstrated as outstanding UV NLO crystals.[10-17] An ideal nonlinear optical (NLO) crystal structure must satisfy at least three essential conditions. First, the crystal must be non-centrosymmetric (NCS), which is a fundamental requirement for possessing a nonzero second-order nonlinear coefficient (d_{ij}) and enabling even-order nonlinear effects under intense laser irradiation (Figure 1A). Second, to achieve efficient second-harmonic generation (SHG), phase matching must be realized. Moderate birefringence is necessary to compensate for phase mismatch over useful coherence lengths; however, excessive birefringence can lead to spatial walk-off between the wave vector and the Poynting vector, thereby reducing conversion efficiency (Figure 1B). Third, the electronic band structure of the crystal, determined by its atomic arrangement, defines its transparency window. The bandgap establishes a cutoff edge, which limits the spectral range over which the crystal can effectively operate (Figure 1C). Organic nonlinear optical (NLO) materials offer advantages such as higher NLO coefficients and greater structural diversity or flexibility.[18,19] However, organic materials also suffer from inherent limitations, including poor physicochemical stability, low mechanical strength, strong absorption in the ultraviolet region, and a tendency toward centrosymmetric crystallization due to strong dipole–dipole interactions. According to previous studies, non-centrosymmetric (NCS) crystal structures are found in only about 20% of molecular organic crystals.[20-22] Therefore, in recent years, significant research efforts have focused on semi-organic NLO materials, aiming to develop superior NLO crystals by combining the strengths of organic and inorganic components.[23-34] Nevertheless, based on our survey and analysis of these semi-organic crystals, issues such as a low proportion of NCS structures, excessively large birefringence, and overly narrow band gaps persist even within this class. Consequently, only L-arginine phosphate (LAP) and its deuterated form, DLAP, have achieved a satisfactory balance among these properties and are commercially used as ultraviolet NLO crystals.[35] In this work, the relevant properties of the synthesized GLM crystal were preliminarily evaluated and compared with those of current mainstream organic and semi-organic optical crystals (Table S1). The results demonstrate that GLM achieves a precise balance among a non-centrosymmetric structure, suitable birefringence for phase-matching, and a bandgap well-matched to the target wavelength range, highlighting its potential value for future applications.

For organic molecular crystals, the formation of NCS crystal structures is facilitated by minimizing dipole-dipole molecular interactions through the reduction of dipole moments in the ground state.[36] Conversely, when substantial permanent dipole moments exist in the ground state, these dipoles tend to repel each other during crystallization. This leads to a natural propensity to form antiparallel molecular dimers or clusters, resulting in unit cells with inversion symmetry that render bulk materials devoid of NLO properties.[37] Moreover, hydrogen bonding networks, anion coordination patterns, solvation history, and crystal growth kinetics are also indispensable factors in determining the final crystal symmetry. Through the strategic structural design of introducing counterions, the dipole interactions (Coulombic forces) between cations and anions will compete with the detrimental dipole interactions among identical organic groups, thereby separating the organic dipole. Furthermore, reducing the ground-state dipole moment of the organic groups also helps to weaken such detrimental dipole interactions. This dual mechanism suppresses the formation of antiparallel dipole dimers within the crystal, which may favor the formation of NCS crystal structures.

Additionally, contrary to common perception, small dipole moments and large first-order molecular hyperpolarizabilities are not incompatible requirements. For charge-transfer molecules, a two-level model links the first-order hyperpolarizability (β) to the dipole moment difference ($\Delta\mu$) between the ground and excited states in first-order nonlinear processes.[38]

$$\beta(-2\omega;\omega;\omega) = \frac{3e^2\hbar W f}{2m\left[W^2-(2\hbar\omega)^2\right]\left[W^2-(2\hbar\omega)^2\right]}\Delta\mu \quad (1)$$

Among them, $\hbar\omega$ is the energy of a laser photon, and W and f represent the energy difference and oscillator strength of the charge transfer transition, respectively. Upon excitation, electrons transition into antibonding orbitals, driving charge transfer from the donor (D) to the acceptor (A) — forming the D→A charge-transfer state. Thus, for NCS molecules with small ground-state dipole moments, possessing a large excited-state dipole moment alone can still ensure substantial first-order hyperpolarizability (β). To verify this, we employed the TD-SCF method to calculate the average electric dipole moments of the $[C_3N_3O_2H_8]^+$ and $[C_3N_3OH_6]^+$ groups in their three lowest-energy singlet excited states (S_1, S_2, and S_3). The results indicate that the $[C_3N_3OH_6]^+$ group, despite having a smaller ground-state dipole moment, still possesses a sufficient $\Delta\mu$. This aligns well with its expected substantial β in Figure 2. It shows the electrostatic potential maps of the organic groups in the S_1 excited state from TD-DFT calculations in Figure S1. Notably, when the incident light frequency approaches the molecular electronic transition

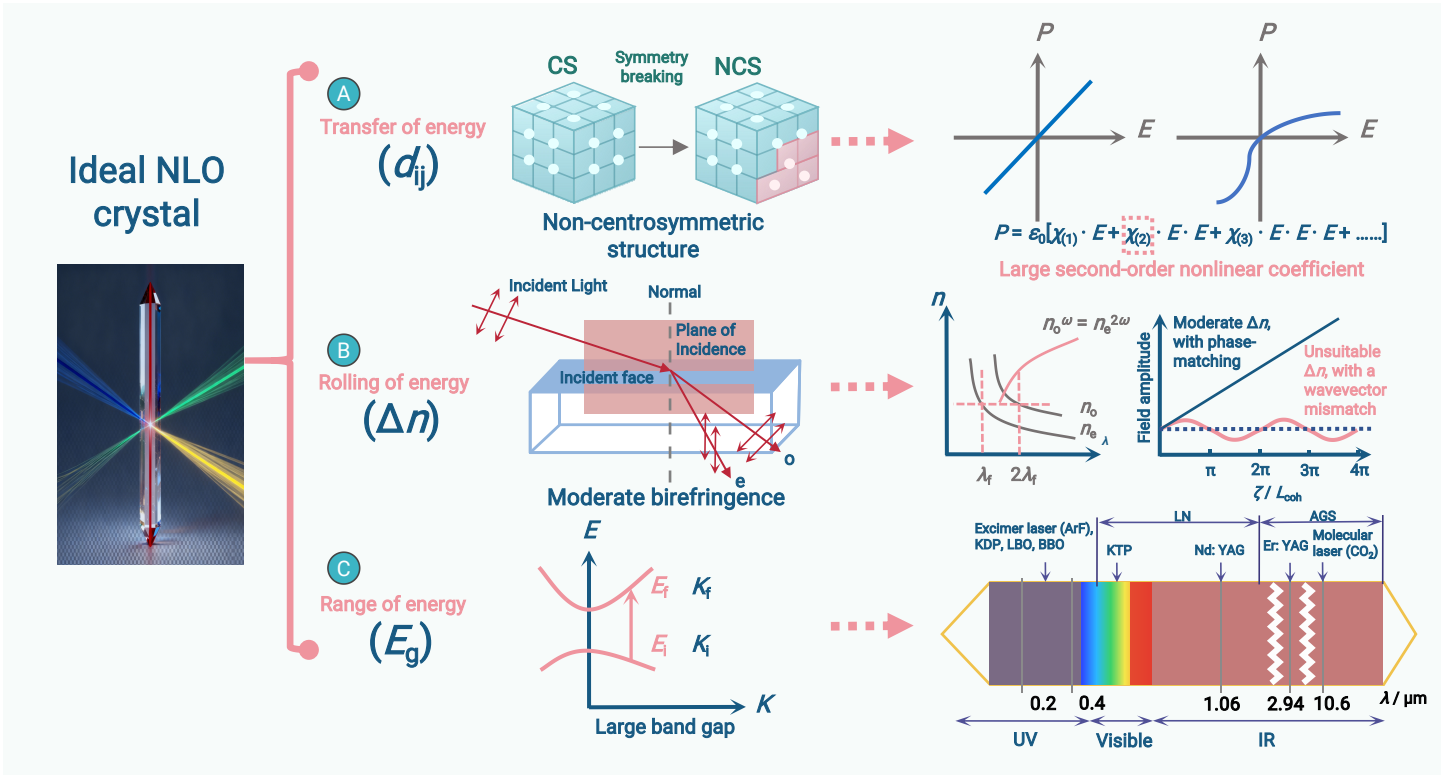

Figure 1. Key performance factors for ideal NLO optical crystals (A) Energy Transfer: The NCS structure and large second-order nonlinear coefficient are essential for enabling second-order nonlinear effects. (B) Energy Rolling: During nonlinear processes, phase mismatch between fundamental and second-harmonic light due to refractive index dispersion is a significant issue. The birefringence of anisotropic crystals can effectively compensate for this phase mismatch. However, excessively small or large birefringence is detrimental. (C) Energy Range: The interaction between photons and the crystal is influenced by the crystal's characteristic band structure, leading to characteristic absorption. The crystal's bandgap directly affects the usable wavelength range.

frequency, the contribution from virtual states to the excited state is significantly amplified, resulting in resonance-enhanced nonlinear responses.

Here, the high second-harmonic generation (SHG) efficiency of organic chromophores and the simplicity of synthesizing semi-organic salts through counterion rearrangement have motivated us to investigate organic salts based on glycocyamine. It was determined that appropriately reducing the ground-state dipole moment of the organic chromophore and introducing counterions can alter the arrangement of a given organic chromophore in the crystal, thereby affecting the symmetry of the crystal structure. The glycocyamine cation demonstrated superior static polarization anisotropy (δ) and hyperpolarizability (β) in the solar-blind UV region (Figure 2A), outperforming many traditional anionic groups and making it a promising novel functional group for NLO applications. Glycocyamidine, formed by the polycondensation of glycocyamine into a ring, has a smaller ground-state dipole moment, while methylsulfonic acid anion, as a counterion, effectively competes with harmful dipole-dipole interactions. The synthesized $(C_3N_3OH_6)(CH_3SO_3)$ (GLM) successfully crystallizes in an NCS space group, achieving a balance among SHG efficiency, birefringence, and bandgap. This compound exhibits a strong phase-matched SHG response (2.0×KDP), significant birefringence (0.078 at 546 nm), and a UV cutoff edge (217 nm). Additionally, first-principles calculations show that the bandgap is primarily determined by the $(C_3N_3OH_6)^+$ cation, while the NLO properties are mainly contributed by the organic moiety (Glycocyamidine). Furthermore, preliminary experiments demonstrate that GLM has excellent crystal growth characteristics, and a single crystal with dimensions of 27×8×7 mm^3 was successfully prepared from room-temperature aqueous solutions.

MATERIALS AND METHODS

Materials

Glycocyamine ($C_3H_7N_3O_2$, 99.5%, Sigma-Aldrich), methanesulfonic acid (99%, Sigma-Aldrich), hydrochloric acid (37%, Aladdin), ethanol (99.5%, Sigma-Aldrich), diethyl ether (99%, Aladdin), and acetone (99%, Aladdin) were used as received without further purification. Deionized water and anhydrous methanol were used as solvents where specified.

Crystal synthesis and growth

HGM crystals $[(C_3N_3O_2H_8)(CH_3SO_3)\cdot H_2O]$ were obtained by dissolving glycocyamine (1.17 g) and anhydrous methanesulfonic acid (1.25 g) in deionized water (20 mL), stirring at 50°C for 30 min, followed by slow evaporation at room temperature; millimeter-sized crystals formed after ~7 days and were washed with anhydrous acetone and dried.

GLM crystals $[(C_3N_3OH_6)(CH_3SO_3)]$ was prepared by (i) an HCl-assisted conversion route (glycocyamine in 6 M HCl, sealed-tube reflux at 120°C with LC-MS monitoring; solvent removal and recrystallization from ethanol/diethyl ether), followed by salting/crystallization with methanesulfonic acid; or (ii) a one-pot methanol route (glycocyamine and methanesulfonic acid in anhydrous methanol under reflux at 120°C, then solvent removal and re-dissolution in methanol, and slow evaporation to crystallize; typical yield ~86%); or (iii) dehydration of HGM (ground HGM heated at 110°C for 24 h) to afford GLM polycrystalline powder.

Single crystals of GLM were grown from a methanol/water mixed solvent by preparing a saturated solution at 60 °C, introducing seed crystals, and cooling at ~1 °C/day.

X-ray diffraction

Single-crystal X-ray diffraction data were collected on a Bruker D8 Venture diffractometer (Mo Kα, λ = 0.71073 Å). Data reduction and absorption correction were performed using SAINT/SCALE, and structures were solved/refined using Olex2 and SHELXTL with full-matrix least-squares refinement on F^2; non-hydrogen atoms were refined anisotropically. PLATON was used for symmetry checks.[39-41]

Powder X-ray diffraction patterns were recorded on a Bruker D2 PHASER diffractometer (Cu Kα, λ = 1.5418 Å) at 300 K over 2θ = 5–70°.

Spectroscopy and thermal analysis

FT-IR spectra were collected on a Shimadzu IR Affinity-1 spectrometer (400–4000 cm^{-1} using KBr pellets (4 mg sample/300 mg dried KBr). UV–vis–NIR transmission spectra of single crystals were measured on a Shimadzu SolidSpec-3700DUV (190–1600 nm), and powder diffuse

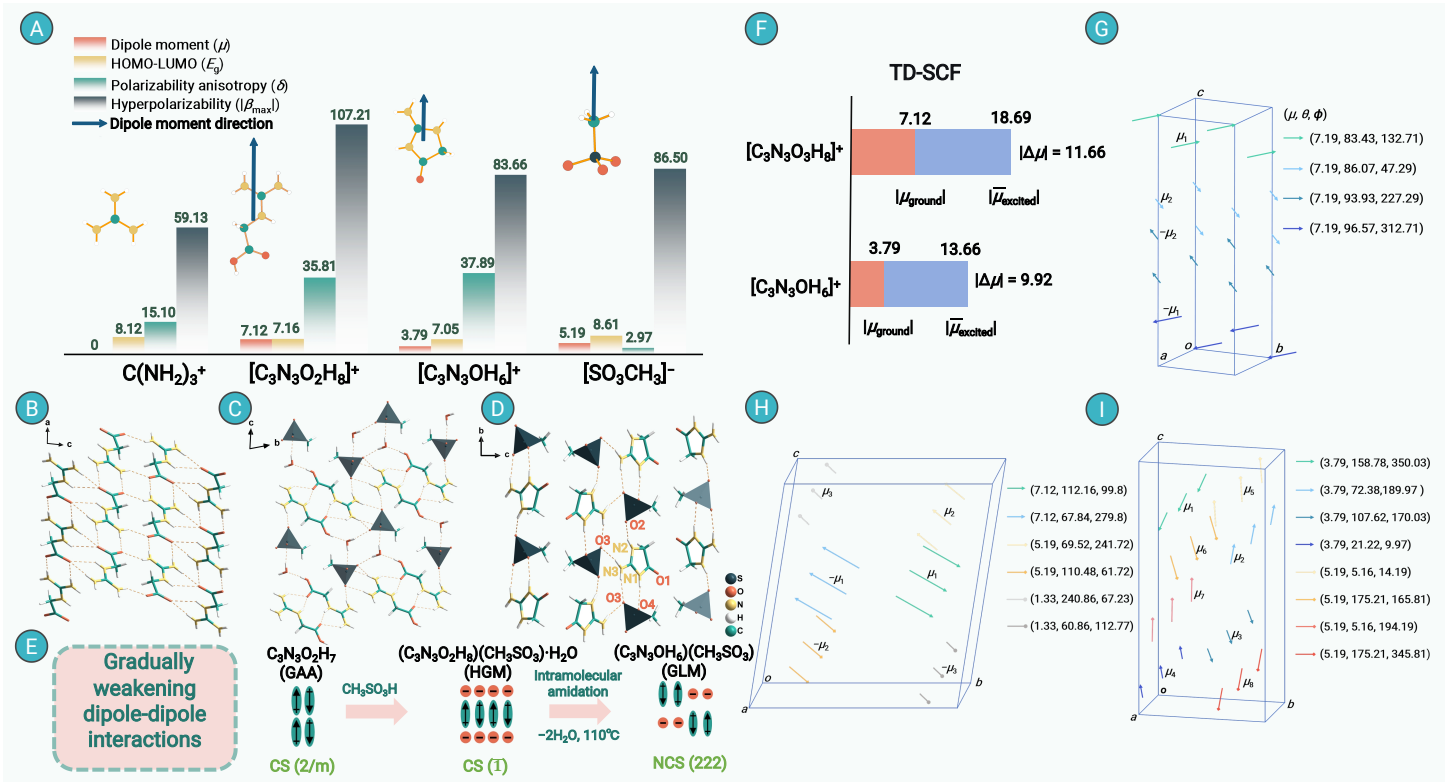

Figure 2. Optical properties of microscopic groups, crystal structural features, and molecular dipole (A) The geometric structures of the involved functional groups and ions, as well as their linear and NLO properties, have been studied. The directions of dipole moments were marked. The calculation was carried out using density functional theory (DFT) implemented by the Gaussian09 package at the 6-31G level.[50] (B-D) The crystal structures of GAA, HGM, and GLM, along with a schematic diagram illustrating molecular dipole-dipole interactions. (E) The dashed lines represent intermolecular hydrogen bonding. Green ellipsoids denote typical dipoles, while orange spheres indicate sterically hindered groups, namely anions. (F) TD-SCF calculations were implemented using the Gaussian 09 package at the 6-31G level. The dipole moment vectors of the three lowest-energy singlet excited states were obtained via TD (NStates = 3) calculations, and the difference between the average dipole moment vector of these three excited states and the ground-state dipole moment was derived $|\Delta\mu| = |\vec{\mu}_{excited} - \mu_{ground}|$. (G-I) represent the dipole vector mappings in the GAA, HGM, and GLM crystals, respectively. In the crystallographic orthogonal coordinate system, spherical coordinates are defined with the polar axis direction taken from the c-axis direction and the X-axis direction taken from the projection of the a-axis onto the XY plane. The spherical coordinates of each dipole vector are annotated. The arrow-shaped vectors correspond to the dipole vectors of the organic groups, the rectangular vectors denote those of the inorganic anions, and the circular vectors represent the dipole vectors of water molecules.

reflectance spectra were measured on the same instrument (190–2600 nm). Optical band gaps were estimated from Kubelka–Munk transformed reflectance data.[42,43]

Thermogravimetry–DSC was performed under flowing N_2 in a Pt crucible from room temperature to 600°C at 5 °C/min.

Birefringence and powder SHG measurements

Birefringence was determined using a Carl Zeiss polarizing microscope (Axioscope 5) with a visible filter via retardation–thickness analysis. Powder second-harmonic generation (SHG) was evaluated using a modified Kurtz–Perry method with a Q-switched Nd: YVO_4 laser (1064 nm).[44] Polycrystalline samples were ground/sieved into defined particle sizes (25–45 to 150–212 μm) and benchmarked against KDP powders in identical size fractions.

Computational methods

Periodic first-principles calculations (band structures, density of states, and optical properties) were performed using CASTEP with the PBE-GGA functional and norm-conserving pseudopotentials. A plane-wave cutoff of 700 eV, SCF convergence of 10^{-6} eV/atom, and Monkhorst–Pack k-point meshes generated from a k-point spacing of 0.06 $Å^{-1}$ were used.[45–48] The GGA–Exp gap difference was applied as a scissor correction for optical-property calculations. Static refractive indices/birefringence were derived from the real part of the dielectric function, and SHG coefficients were computed using the length-gauge formalism (Aversa–Sipe, $\omega \to 0$ limit).[49]

Molecular-level calculations were performed in Gaussian 09 at the 6-31G level.[50] Orbitals and polarizability anisotropy of ionic groups were evaluated using B3LYP/6-31G. Excited-state permanent dipole moments ($S_1 - S_3$) were computed using TD-SCF/6-31G based on RHF/6-31G optimized ground-state geometries (tight SCF/optimization and no symmetry constraints); dipole moments were reported in Debye.[51,52] Unless otherwise stated, these excited-state dipoles were obtained for isolated molecules (gas-phase model without implicit solvent or explicit crystal embedding).

RESULTS AND DISCUSSION

Owing to the multifunctionality of the guanidinium group, molecules may undergo intermolecular condensation polymerization (crosslinking) or intramolecular cyclization (non-crosslinking). For instance, the chemical transformation of creatine into creatinine via non-enzymatic dehydration involves the reaction between the guanidinium group (–NH–C(=NH)–NH–CH_3, derived from arginine) and the carboxyl group (–CH_2–COOH, from glycine). Mechanistically, the imino nitrogen (–NH–) of the amidine group acts as a nucleophile attacking the carbonyl carbon (C=O) of the carboxyl group, leading to the elimination of a water molecule (H_2O). This results in a new C–N bond formation, converting creatine into cyclic creatinine—a 5-membered lactam structure containing two nitrogen atoms (one amido –NH– and one imino –N=), a carbonyl (C=O), with the methyl side chain retained. This reaction is irreversible. Guanidinoacetic acid (GAA), as the precursor to methylated creatine, exhibits analogous cyclization reactivity. Detailed synthetic procedures are provided in the Supporting Information (SI), with phase purity confirmed by PXRD (Figure 3A). The resulting GLM compound demonstrates excellent solubility in polar solvents (e.g., water and methanol) with minimal hydrolysis, facilitating the growth of large single crystals. GLM crystals exhibit remarkable stability under ambient conditions, resisting decomposition, oxidation, and moisture absorption. Thermogravimetric-differential scanning calorimetry (TG-DSC) data indicate that GLM maintains thermal stability up to 196°C (Figure S2). Notably, ($C_3N_3O_2H_8$)(CH_3SO_3)·H_2O (HGM) displays similar endothermic peaks near 196 and 320 °C on its DSC curve, suggesting that GLM can be directly obtained from HGM via thermal dehydration. This was experimentally verified by XRD analy-

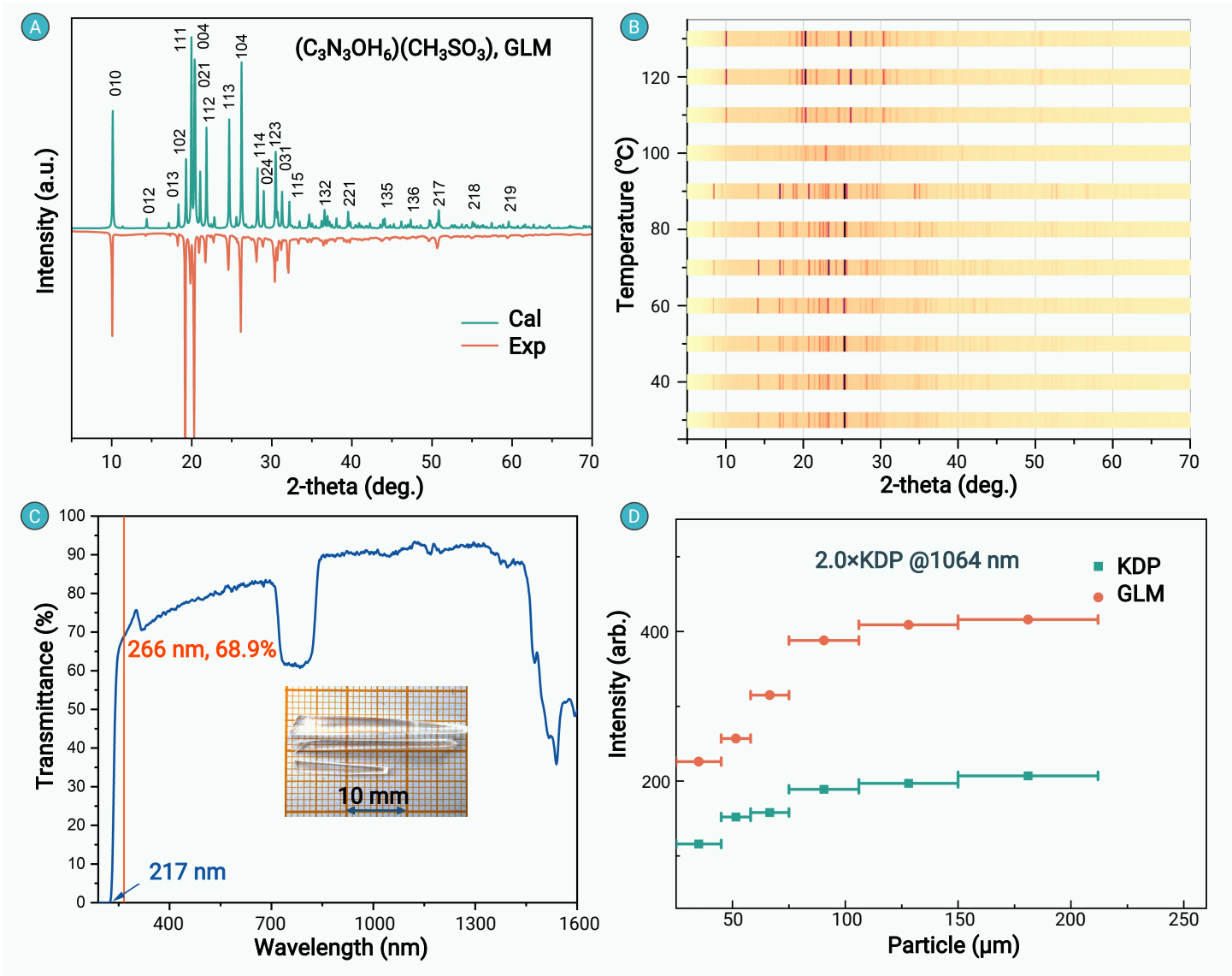

Figure 3. Some related properties of the GLM crystal (A) PXRD patterns. (B) Variable-temperature XRD patterns from 30 to 130°C, representing the transformation from HGM to GLM under thermally induced dehydration. (C) UV-vis-NIR transmittance spectra. (D) Polycrystalline powder SHG intensity curve at 1064 nm.

sis of HGM after heating at 110°C (Figure S3), confirming the phase transition. Furthermore, GLM undergoes acid-catalyzed ring-opening hydrolysis in aqueous solution to regenerate HGM, enabling facile interconversion between CS and NCS compounds.

Figure 2B illustrates the crystal structure of guanidinoacetic acid (GAA). It crystallizes in the CS monoclinic space group $P2_1/c$ (No. 14), with lattice parameters a = 9.846(3) Å, b = 8.176(3) Å, c = 10.885(3) Å, β = 100.182(13)°, and unit cell volume V = 862.5(5) Å^3 (Table S2). As a typical covalent molecular organic crystal, GAA possesses a significant molecular dipole moment. The molecules are anchored via strong dipole-dipole interactions, forming a characteristic antiparallel arrangement of dipolar molecules. This configuration strongly drives the formation of CS crystallization. Generally, dipolar ionic compounds tend to crystallize in NCS space groups more readily than dipolar covalent compounds. For more details on crystallography, please refer to Table S3-S7.Furthermore, to more accurately assess the types, orientations, and interaction energies of dipole vectors within the crystals, detailed dipole vector maps for the three crystals are provided in Figures 2G-I. Considering that the dipole length (l) and the distance between neighboring dipoles (r) are comparable in the evaluation of their interaction energy, an extended dipole model under polar coordinate projection was employed to calculate the interaction energy (U) between nearest-neighbor dipoles, providing an approximate assessment of dipole interaction strength (Table S8). Taking GAA as an example, four typical dipole orientations exist within the crystal, with the strongest interaction energy being $U_{\mu1\sim-\mu1}$ = −0.481 (Hartree atomic units, 1 a.u. of $U = E_h$). However, considering the ionic compounds discussed later, it is reasonable to hypothesize that the counterions favor a parallel arrangement of the dipolar cationic groups to maximize the Madelung stabilization energy. To verify the existence of such an arrangement in dipolar ionic crystals, we determined the following crystal structure. Figure 2C depicts the crystal structure of the synthesized hydrated glycocyamine mesylate (HGM). It crystallizes in the CS triclinic space group $P\bar{1}$ (No. 2), with lattice parameters a = 5.1109(8) Å, b = 9.6458(12) Å, c = 10.8864(16) Å, α = 74.741(5)°, β = 79.878(6)°, γ = 79.223(5)°, and unit cell volume V = 504.08(13) Å^3 (Table S2). The asymmetric unit contains one $(C_3N_3O_2H_8)^+$ cation, one $(CH_3SO_3)^-$ anion, and one H_2O molecule. The $(C_3N_3O_2H_8)^+$ cations and $(CH_3SO_3)^-$ anions interact via electrostatic Coulombic attraction and strong hydrogen bonding. The $(C_3N_3O_2H_8)^+$ cations arrange via π-π stacking interactions, forming a quasi-two-dimensional layered structure, with the $(CH_3SO_3)^-$ anions intercalated between them. Given this pronounced orientation within the crystal, a large birefringence is anticipated. Despite the introduction of the $(CH_3SO_3)^-$ anion, which creates dipole competition, the strong dipole–dipole interactions between $(C_3N_3O_2H_8)^+$ cations still promote the formation of distinct antiparallel dimers, with the strongest interaction energy being $U_{\mu1\sim-\mu1}$ = −0.328. This arrangement is unfavorable for NCS crystallization. Figure 2D presents the crystal structure of Glycocyamidine mesylate (GLM). GLM crystallizes in the chiral orthorhombic space group $P2_12_12_1$ (No. 19), with lattice parameters a =

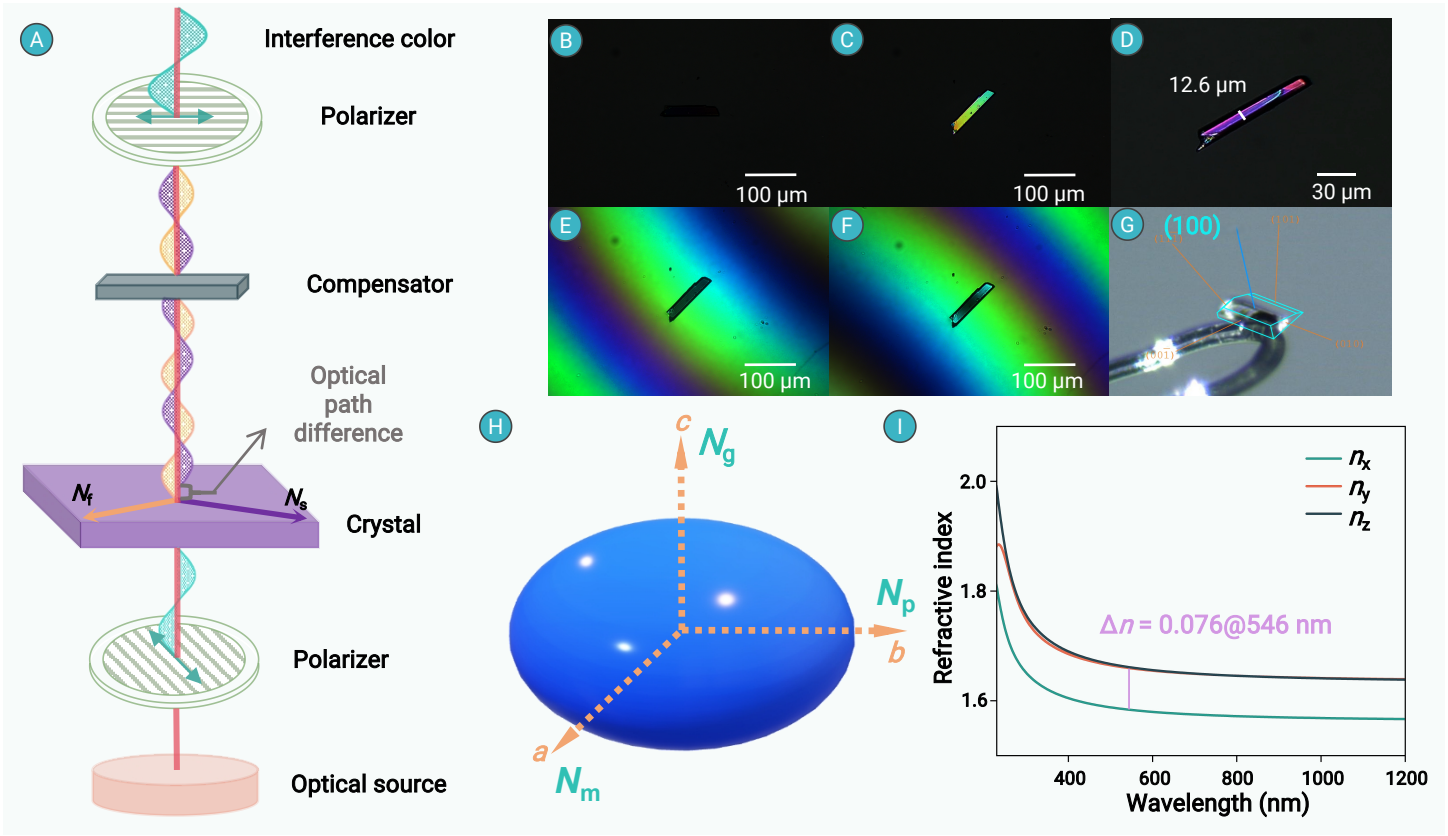

Figure 4. Birefringent properties of GLM (A) Schematic diagram of the birefringence test. (B) Crystal achieves complete extinction. (C). Original interference color of GLM. (D) Thickness of the measured plate. (E and F) Positive and negative rotation of the compensator. (G) Crystal orientation of GLM sample determined by single-crystal XRD. (H) Triaxial ellipsoid of three principal refractive indices. (I) Theoretical calculation result of the wavelength-dependent refractive indices.

5.4142(5) Å, *b* = 8.6892(7) Å, *c* = 17.4413(14) Å, and unit cell volume *V* = 820.53(13) Å^3 (Table S2). The asymmetric unit contains one $(C_3N_3OH_6)^+$ cation and one $(CH_3SO_3)^-$ anion. The $(C_3N_3OH_6)^+$ cation is derived from the dehydration and condensation of the $(C_3N_3O_2H_8)^+$ cation under acidic conditions. Its five-membered ring is strain-free and conformationally stable, leading to a low transition state energy, a favorable entropy change, and high reaction efficiency. The synthesized $(C_3N_3OH_6)^+$ cation possesses a smaller static dipole moment (3.79 Debye) and a larger β value (83.66) (Figure 2A). The reduced dipole moment of this group weakens the dipole-dipole interactions between cations in the GLM crystal (U_{max} = −0.082, significantly smaller than the U_{max} values in GAA and HGM). Competitive dipole interactions are observed between the cations and anions (U_{max} = −0.075). The fundamental structure illustrated in Figure 2D is consistent with the results of the aforementioned analysis. This dual effect of dipole weakening and dipole competition prevents the $(C_3N_3OH_6)^+$ cations from adopting an antiparallel dimerization mode, resulting in four entirely distinct cation orientations, as shown in Figure 2I. Furthermore, the cation possesses an intramolecular charge-transfer (ICT) axis N1−O3 at an appropriate position. The delocalization of electron density along this charge-transfer axis will determine its $\chi^{(2)}$ tensor. Each $(C_3N_3OH_6)^+$ cation connects to three adjacent $(CH_3SO_3)^-$ anions via N1−H1···O4, N2−H2···O3, and N3−H3···O3 hydrogen bonds (Figure 2D), while each $(CH_3SO_3)^-$ anion is fixed by three $(C_3N_3OH_6)^+$ cations, forming a strong hydrogen-bonded network. The bond lengths of these hydrogen bonds range from 2.790 to 2.840 Å (Table S6), indicating fairly strong bonding strength. Other longer interatomic distances correspond to expected van der Waals contacts. Interactions between $(CH_3SO_3)^-$ anions themselves and between $(C_3N_3OH_6)^+$ cations occur primarily via dipole interactions, as they lie beyond typical hydrogen-bonding distances. Through the introduction of dipole interactions between cations and anions to compete with the undesirable dipole interactions of antiparallel dimers, supplemented by hydrogen bonding, this principle is analogous to using cocrystal design concepts to generate NCS 2D assemblies.[53] Specifically, it involves the formation of NCS structures through the hydrogen bond-directed association of specific groups. Our results demonstrate that the dual strategy of introducing counterions to induce dipole competition and reducing the molecular ground-state dipole moment can effectively weaken the detrimental dipole interactions and direct the self-assembly of functional groups into NCS structures, as supported by our experimental evidence. Furthermore, this "organic salt approach" also facilitates the preparation of NLO crystals with significant $\chi^{(2)}$ values. Moreover, as the dipole-dipole interactions weaken progressively from GAA to HGM to GLM, the growth of single crystals from aqueous solution becomes easier. This is likely because compounds with strong dipole interactions in solution require overcoming a higher energy barrier for crystallization. Consequently, the growth of large GLM single crystals holds considerable promise. overcoming a larger energy barrier. Therefore, the growth of large GLM single crystals holds significant promise.

Pure phases of HGM and GLM were successfully synthesized. All peaks in their powder X-ray diffraction (PXRD) patterns match perfectly (Figure 3A). For GLM crystallizing in the $P2_12_12_1$ space group, the absence of (*h*00) (*h* = 2*n* + 1) diffraction peaks is a necessary consequence of systematic absences, arising from its three 2_1 screw axes of symmetry. The continuous variable-temperature XRD analysis of HGM from 30 to 130°C was conducted. As shown in Figure 3B, the characteristic main peak of GLM appears at approximately 110°C, indicating the phase transition temperature, which is consistent with the TG-DSC results. GLM, as a UV NLO crystal, exhibits excellent potential in both linear and NLO responses. An unpolished GLM crystal wafer (1 mm thick) displays a UV-Vis-NIR transmission window covering the wavelength range of 217–1600 nm (Figure 3C), satisfying a key requirement for its application in the UV region. In contrast, the CS HGM crystal shows an optical band gap of 5.69 eV (Figure S4). Furthermore, the characteristic absorption peaks in the infrared (IR) spectra of GLM and HGM compounds, along with their corresponding vibrational assignments, are labeled in Figure S5. Belonging to an NCS space group, GLM is theoretically capable of a SHG response. Its SHG efficiency was quantified using the Kurtz-Perry powder method[44] under 1064 nm fundamental radiation, with KDP as the reference standard. As shown in Figure 3D, the SHG intensities of GLM increase with

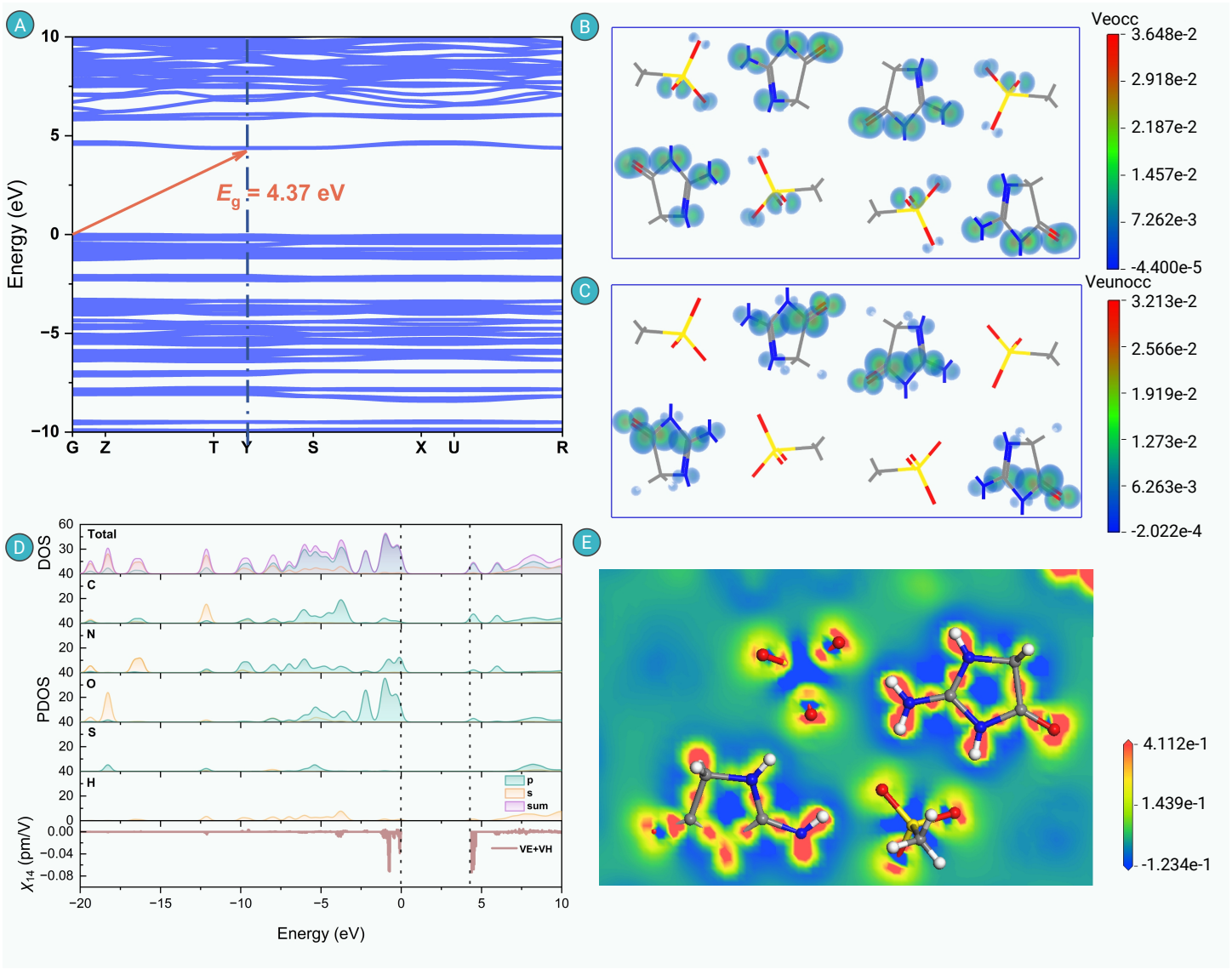

Figure 5. Theoretical calculations of GLM (A) Band structure using the GGA method. (B-C) SHG-weighted densities of occupied and unoccupied states in the virtual electron process. (D) Total and partial densities of states. (E) Electron density difference map.

particle size until reaching a plateau at a critical particle size of 150–212 μm. This size-independent behavior confirms their type-I phase-matching capability at 1064 nm wavelengths. Notably, at the maximum particle size, GLM exhibits a 1064 nm SHG efficiency 2.0 times that of commercial KDP. These results demonstrate that GLM exhibits both high SHG efficiency and a wide transparent window, making it an exceptional candidate material for all-solid-state compact UV laser systems.

Birefringence, as another key optical property, plays a crucial role in the phase-matching of NLO crystals. Its essence is intimately related to the optical anisotropy of the crystal. At a wavelength of 546 nm, the birefringence of GLM was tested using a micron-thick wafer of a single GLM crystal on a Carl Zeiss polarizing microscope (Axioscope 5). As shown in Figure 4, when linearly polarized light passes through the GLM crystal and is then viewed through a second polarizer crossed perpendicularly to the first, typical colored images are observed. This interference effect arises from the optical path difference between the ordinary and extraordinary rays. As the crystal is rotated, the image brightness changes periodically from darkest to brightest and back to darkest every 45°. Complete extinction images occur when the polarization direction of the incident light is parallel to either the fast or slow axis of the single crystal, resulting in zero optical path difference. These results demonstrate that the GLM crystal possesses significant anisotropic refractive indices, confirming it is a birefringent crystal. The calculated birefringence, determined using the plane-wave pseudopotential method within the CASTEP software package[45,46,49,54,55], reveals that GLM exhibits a suitable birefringence of Δn = 0.076 at 546 nm (Figure 4I). A set of refractive indices on the crystal faces of GLM was also calculated to visualize the optical indicatrix, which displays the refractive index for light vibrating in any direction. For GLM (a biaxial crystal), the axis of minimum refractive index (Np) aligns with the crystallographic b axis, while the principal optical axes Ng and Nm align with the crystal c axis and a axis, respectively (Figure 4H). This implies that the maximum birefringence of the GLM crystal should theoretically be measurable on the (100) crystal face. Accurate optical path differences were measured by using a Berek compensator to cancel the path difference between the ordinary and extraordinary rays (Figures 4E-F). The crystal orientation used for testing was verified by single-crystal X-ray diffraction (Figure 4G); the selected crystal face was oriented along the (100) direction, with a thickness d = 12.6 μm. According to crystal optics theory, the polarization effect can be calculated using the corresponding formula (SI). The experimentally measured birefringence value for the GLM crystal at 546 nm is 0.078, which matches the calculated value. This birefringence value is lower than that of most organic-inorganic hybrid crystals, which helps avoid beam walk-off effects. Assisted by density functional theory (DFT) calculations, quantitative contribution analysis of individual units via the real-space atom cutting method (Table S9) confirms that the π-conjugated $(C_3N_3OH_6)^+$ cations are the primary contributors to the birefringence of the GLM crystal. Furthermore, the projections of the linear groups within the conjugated plane of the

$(C_3N_3OH_6)^+$ cation hardly align along the b direction. This alignment leads to lower electron density in this direction, thus resulting in a smaller refractive index compared with other orientations. In contrast, the projections along the *a* and *c* axes lack this collinearity. Because of this, the refractive indices along these axes are similar and are both significantly higher than that along the *b* direction. This difference provides the material with sufficient birefringence. Additionally, the non-coplanar arrangement of the two sets of $(C_3N_3OH_6)^+$ cations, each with parallel in-plane alignment, suppresses the possibility of excessively high birefringence, keeping the overall birefringence at a moderate level. Similarly, the birefringence of the HGM crystal was also calculated and measured (SI). As HGM crystallizes in a triclinic CS space group, the principal axes of its optical indicatrix exhibit significant angular deviations from all three crystallographic axes. Consequently, it is difficult to find a high-index natural crystal face suitable for measuring the maximum birefringence. We measured the birefringence on the $(00\bar{1})$ face of the HGM crystal, obtaining Δn = 0.12. The discrepancy between this value and the calculated value of 0.14 is attributed to the angular deviation between the measurement direction and the principal optical axes. Nevertheless, it also verifies to a certain extent that the HGM crystal has a large birefringence, which is attributed to the almost unidirectional arrangement of the projections of linear groups within the conjugated planes of the π-conjugated $(C_3N_3O_2H_8)^+$ cations, suggesting that the HGM crystal therefore holds potential as a UV birefringent crystal.

To elucidate the structure-property relationships governing the optical properties of compound GLM, we performed first-principles calculations using the CASTEP package.[45] As shown in Figure 5A, electronic band structure calculations employing the generalized gradient approximation (GGA) with the Perdew-Burke-Ernzerhof functional[56] reveal an indirect band gap of 4.37 eV, with systematic underestimation due to self-interaction error inherent in semi-local functionals. The band gap difference between GGA and experimental value served as a scissors operator for computing birefringence and SHG coefficients.[57] Density of states (DOS) and projected DOS analyses (Figure 5D) indicate that H 1s, S 3s, and S 3p orbitals reside far from the Fermi level, while C 2p, N 2p, and O 2p orbitals dominate the upper region of the valence band and the lower region of the conduction band. Strong covalent bonding within the $(C_3N_3OH_6)^+$ ring arises from significant hybridization of C, N, and O orbitals. Electron density difference map (EDDM) analysis (Figure 5E) further demonstrates an asymmetric $\Delta\rho$ distribution along polar directions in the $(C_3N_3OH_6)^+$ cation, indicating a strong charge transfer channel that dominates the SHG response. The non-coplanar arrangement of two conjugated groups disperses electron density, preventing excessive Δn. These analyses confirm the $(C_3N_3OH_6)^+$ ring as the primary NLO chromophore, critically governing both microscopic birefringence origins and NLO response. Non-covalent interactions drive the dual planar alignment of these rings, modulating birefringence, while valence electrons near the band gap determine the second-order susceptibility. For GLM's 222 point group structure, Kleinman symmetry constraints yield only one independent SHG tensor component (d_{14} = d_{25} = d_{36}). Within the independent-particle approximation and length-gauge formalism, we computed its SHG tensor, obtaining a maximum static $|d_{14}|$ value of 0.89 pm/V – notably exceeding KDP's $|d_{36}|$ (0.39 pm/V). Orbital-resolved SHG-density analysis (Figures 5B-C) reveals virtual electron (VE) processes dominate the SHG response (> 80% contribution), with negligible virtual hole (VH) involvement. For d_{14} in VE-occupied states, SHG primarily originates from C 2p, N 2p, and O 2p orbitals in the π-conjugated $(C_3N_3OH_6)^+$ cation, with minor contributions from O 2p orbitals in the non-π-conjugated $(CH_3SO_3)^-$ anion. In VE-unoccupied states, SHG arises almost exclusively from band-edge orbitals (C 2p, N 2p, O 2p) of the π-conjugated cation, consistent with recent studies on NCS sublattice contributions.[58] Quantitative real-space atom-cutting analysis[59] (Table S9) confirms the π-conjugated $(C_3N_3OH_6)^+$ cation as the dominant contributor to the SHG coefficient, while both cations and anions contribute to GLM's moderate birefringence. In summary, GLM's strong SHG originates from the coherent superposition of hyperpolarizabilities within the π-stacked organic cations, with $(C_3N_3OH_6)^+$ serving as the NLO-active chromophore. Crucially, the non-π-conjugated $(CH_3SO_3)^-$ anion promotes non-coplanar alignment of the two $(C_3N_3OH_6)^+$ cations (each maintaining in-plane parallelism), suppressing excessive birefringence while maintaining optimal Δn.

CONCLUSION

In summary, this study addresses the common challenge in covalent molecular crystals, where strong dipole-dipole interactions driven by large molecular dipole moments often lead to antiparallel dimerization and, consequently, centrosymmetric crystallization. We propose a dual molecular engineering strategy—namely, "dipole weakening" and "dipole competition"—to guide the self-assembly of functional groups and circumvent symmetry traps, and provide a semi-quantitative analysis of the dipole arrangement mechanism in the presence of counterions and weakened dipole moments. Based on this strategy, a novel NLO material, GLM, was obtained through the thermal dehydration of the synthesized centrosymmetric compound HGM, marking the first successful identification of the $(C_3N_3OH_6)^+$ cation as an NLO chromophore. This material exhibits outstanding comprehensive performance in the solar-blind ultraviolet region, including a second-harmonic generation response approximately 2.0 times that of KDP, a suitable birefringence (Δn = 0.078@1064 nm), a high decomposition temperature (196°C) among semi-organic crystals, and a broad transmission window (0.22–1.60 μm), making it highly competitive compared to the currently sole commercialized semi-organic crystal, LAP. Theoretical calculations reveal that its moderate optical anisotropy stems from the synergistic effect of the non-coplanar arrangement of two sets of $(C_3N_3OH_6)^+$ cations and the coordination by the non-π-conjugated $(CH_3SO_3)^-$ anion, while the strong SHG response originates almost exclusively from the $(C_3N_3OH_6)^+$ cations. This work not only reports a high-performance candidate for UV NLO applications but also, through the dual strategy of "dipole weakening" and "dipole competition," explores the relationship between dipole interactions and symmetry breaking, establishing a new paradigm for designing non-centrosymmetric semi-organic functional crystals. Future work will focus on in situ monitoring of the crystallization process, systematically varying solvents and counterions, and conducting polymorph screening experiments to decouple further the relative contributions of thermodynamic driving forces and kinetic factors in determining symmetry. Additionally, the synthesis and characterization of a wider range of structurally diverse semi-organic compounds will be undertaken to systematically validate and extend this design rationale, providing a more comprehensive verification of the proposed strategy.

REFERENCES

1. Chen C., Wang Y., Wu B., et al. (1995). Design and synthesis of an ultraviolet-transparent nonlinear optical crystal $Sr_2Be_2B_2O_7$. *Nature* **373**:322–324. DOI:10.1038/373322a0
2. Cyranoski D. (2009) Materials science: China's crystal cache. *Nature* **457**:953–955. DOI:10.1038/457953a
3. Dang J., Mei D., Wu Y., et al. (2021). A comprehensive survey on nonlinear optical phosphates: Role of multicoordinate groups. *Coord. Chem. Rev.* **431**:213692. DOI:10.1016/j.ccr.2020.213692
4. Eaton D. F. (1991). Nonlinear optical materials. *Science* **253**:281–287. DOI:10.1126/science.253.5017.281
5. Tran T. T., Yu H., Rondinelli J. M., et al. (2016). Deep ultravioletn onlinear optical materials. *Chem. Mater.* **28**:5238-5258. DOI:10.1021/acs.chemmater.6b02366
6. Wu L., Patankar S., Morimoto T., et al. (2017). Giant anisotropic nonlinear optical response in transition metal monopnictide Weyl semimetals. *Nat. Phys.* **13**:350–355. DOI:10.1038/nphys3969
7. Savage N. (2006). Ultraviolet lasers. *Nat. Photonics* **1**: 83–85. DOI: 10.1038/nphoton.2006.95
8. Shao M., Liang F., Yu H., et al. (2020). Pushing periodic-disorder-induced phase matching into the deep-ultraviolet spectral region: Theory and demonstration. *Light: Sci. Appl.* **9**:45. DOI:10.1038/s41377-020-0281-4
9. Wu Y., Cui C., Wang Z., et al. (2025). Finding a novel borate ferroelectric with random domain structures for deep-UV quasi-phase-matching. *Adv. Mater.* **33**:2505930. DOI:10.1002/adma.202505930
10. Deng Y. L., Hu C. L., Xu X., et al. (2025). $Na[B_3IO_7(OH)]$ and $Na_2[B_4IO_9](IO_3)$: Explorations of boroiodates with strong second harmonic generation response and large birefringence. *J. Am. Chem. Soc.* **147**:12858–12865. DOI:10.1021/jacs.5c01673
11. Jin C., Li Y., Kim J. S., et al. (2025). Exceptional second harmonic generation in ultraviolet nonlinear optical oxyfluoroniobate crystals via structural fingerprint optimization of polar chains. *Angew. Chem., Int. Ed.* **36**: e202512618. DOI:10.1002/anie.202512618
12. Mutailipu M., Zhang M., Wu H., et al. (2018). $Ba_3Mg_3(BO_3)_3F_3$ polymorphs with reversible phase transition and high performances as ultraviolet nonlinear optical materials. *Nat. Commun.* **9**:3089. DOI:10.1038/s41467-018-05575-w
13. Mutailipu M., Zhang M., Zhang B., et al. (2018). $SrB_6O_7F_3$ functionalized with $[B_5O_9F_3]^{6-}$ chromophores: Accelerating the rational design of deep-ultraviolet nonlinear optical materials. *Angew. Chem. Int. Ed.* **57**:6095–6099. DOI:10.1002/anie.201802058

14. Shi G., Wang Y., Zhang F., et al. (2017). Finding the next deep-ultraviolet nonlinear optical material: $NH_4B_4O_6F$. *J. Am. Chem. Soc.* **139**:10645–10648. DOI:10.1021/jacs.7b05943
15. Tran T. T., Koocher N. Z., Rondinelli J. M., et al. (2017). Beryllium-free β-$Rb_2Al_2B_2O_7$ as a possible deep-ultraviolet nonlinear optical material replacement for $KBe_2BO_3F_2$. *Angew. Chem. Int. Ed.* **56**:2969–2973. DOI:10.1002/anie.201612236
16. Wang X., Wang Y., Zhang B., et al. (2017). CsB_4O_6F: A congruent-melting deep-ultraviolet nonlinear optical material by combining superior functional units. *Angew. Chem. Int. Ed.* **56**:14119–14123. DOI:10.1002/anie.201708231
17. Zhang B., Shi G., Yang Z., et al. (2017). Fluorooxoborates: Beryllium-free deep-ultraviolet nonlinear optical materials without layered growth. *Angew. Chem. Int. Ed.* **56**:3916–3919. DOI:10.1002/anie.201700540
18. Liang H., Yang Y., Shao L., et al. (2023). Nanoencapsulation-induced second harmonic generation in pillararene-based host–guest complex cocrystals. *J. Am. Chem. Soc.* **145**:2870–2876. DOI:10.1021/jacs.2c10674
19. Wang Z., Han W., Fu B., et al. (2025). Mechanical twisting-induced enhancement of second-order optical nonlinearity in a flexible molecular crystal. *J. Am. Chem. Soc.* **147**:2766–2775.DOI:10.1021/jacs.4c15519
20. Curtin D. Y. and Paul I. C. (1981). Chemical consequences of the polar axis in organic solid-state chemistry. *Chem. Rev.* **81**:525–541. DOI:10.1021/cr00046a001
21. Gavezzotti A. and Simonetta M. (1982). Crystal chemistry in organic solids. *Chem. Rev.* **82**:1–13. DOI:10.1021/cr00047a001
22. Zyss J., Nicoud, J. F. and Coquillay M. (1984). Chirality and hydrogen bonding in molecular crystals for phase-matched second-harmonic generation: N-(4-nitrophenyl)-(L)-prolinol (NPP). *J. Chem. Phys.* **81**:4160–4167. DOI:10.1063/1.448134
23. Chen Q. Q., Hu C. L., Chen J., et al. (2021). [o-$C_5H_4NHOH]_2[I_7O_{18}(OH)]{\cdot}3H_2O$: An organic–inorganic hybrid SHG material featuring an $[I_7O_{18}(OH)]$ branched polyiodate chain. *Angew. Chem. Int. Ed.* **60**:17426–17429. DOI:10.1002/anie.202106335
24. Kang Y. and Wu Q. (2024). A review of the relationship between the structure and nonlinear optical properties of organic-inorganic hybrid materials. *Coord. Chem. Rev.* **498**:215458. DOI:10.1016/j.ccr.2023.215458
25. Kim K., Li Y. and Ok K. M. (2025). Hafnium-based chiral 2D organic–inorganic hybrid metal halides: Engineering polarity and nonlinear optical properties via para-substituent effects. *J. Am. Chem. Soc.* **147**:2880–2888. DOI:10.1021/jacs.4c16985
26. Li Y., Huang W., Zhou Y., et al. (2023). A high-performance nonlinear optical crystal with a building block containing expanded π-delocalization. *Angew. Chem. Int. Ed.* **62**:e202215145. DOI:10.1002/anie.202215145
27. Xu G., Feng J., Zhang L., et al. (2026). Local conformational confinement and dipole engineering for phase-matchable solar-blind ultraviolet nonlinear optical crystals. *J. Am. Chem. Soc.* **148**:16515–16522. DOI:10.1021/jacs.6c05196
28. Mutailipu M., Han J., Li Z., et al. (2023). Achieving the full-wavelength phase-matching for efficient nonlinear optical frequency conversion in $C(NH_2)_3BF_4$. *Nat. Photonics* **17**:694–701. DOI:10.1038/s41566-023-01228-7
29. Nagapandiselvi P., Baby C. and Gopalakrishnan R. (2015). Synthesis, growth, structure, and nonlinear optical properties of a semiorganic 2-carboxy pyridinium dihydrogen phosphate single crystal. *Opt. Mater.* **47**:398–405. DOI:10.1016/j.optmat.2015.06.012
30. Wang Y., Nisbet M. L., Kamp K. R., et al. (2023). Beyond π–π stacking: Understanding inversion symmetry breaking in crystalline racemates. *J. Am. Chem. Soc.* **145**:16879–16888. DOI:10.1021/jacs.3c05380
31. Wu L., Lin C., Tian H., et al. (2024). $Mg(C_3O_4H_2)(H_2O)_2$: A new ultraviolet nonlinear optical material derived from $KBe_2BO_3F_2$ with high performance and excellent water-resistance. *Angew. Chem. Int. Ed.* **63**:e202315647. DOI:10.1002/anie.202315647
32. Xu G., Bai X., Yang Z., et al. (2025). π-conjugated cations in phosphates: A pathway to solar-blind UV nonlinear optical crystals with phase-matching. *Angew. Chem. Int. Ed.* **38**:e202510363. DOI:10.1002/anie.202510363
33. Xu G., Hu C., Li H., et al. (2025). Improving the performance of birefringent crystals by molecular assembly strategy in the solar-blind UV region. *Small* **21**:2504184. DOI:10.1002/smll.202504184
34. Zhang Z. P., Liu X., Wang R. X., et al. (2024). Remarkable second harmonic generation response in $(C_5H_6NO)^+(CH_3SO_3)^-$: Unraveling the role of hydrogen bond in thermal driven nonlinear optical switch. *Angew. Chem. Int. Ed.* **63**:e202408551. DOI:DOI:10.1002/anie.202408551
35. Jiang M. H. and Fang Q. (1999). Organic and semiorganic nonlinear optical materials. *Adv. Mater.* **11**:1147–1151. DOI:10.1002/(SICI)1521-4095(199909)11:13<1147::AID-ADMA1147>3.0.CO;2-H
36. Zyss J., Chemla D. S. and Nicoud J. F. (1981). Demonstration of efficient nonlinear optical crystals with vanishing molecular dipole moment: Second-harmonic generation in 3-methyl-4-nitropyridine-1-oxide. *J. Chem. Phys.* **74**:4800–4811. DOI:10.1063/1.441759
37. Marder S. R., Perry J. W. and Schaefer W. P. (1989). Synthesis of organic salts with large second-order optical nonlinearities. *Science* **245**:626–628. DOI:10.1126/science.245.4918.626
38. Oudar J. L. and Chemla D. S. (1977). Hyperpolarizabilities of the nitroanilines and their relations to the excited state dipole moment. *J. Chem. Phys.* **66**:2664–2668. DOI:10.1063/1.434213
39. SAINT, Version 7.60A. (2008). Bruker Analytical X-Ray Instruments, Inc., Madison, WI.
40. Dolomanov O. V., Bourhis L. J., Gildea R. J., et al. (2009). OLEX2: A complete structure solution, refinement and analysis program. *J. Appl. Crystallogr.* **42**:339-341. DOI:10.1107/S0021889808042726
41. Sheldrick G. M. (2008). A short history of SHELX. *Acta Crystallogr. A* **64**:112–122. DOI:10.1107/S0108767307043930
42. Kubelka P. and Munk F. Z. (1931). A contribution to the optics of pigments. *Technol. Phys.* **12**:593–603.
43. Tauc J. (1970). Absorption edge and internal electric fields in amorphous semiconductors. *Mater. Res. Bull.* **5**:721–729. DOI:10.1016/0025-5408(70)90112-1
44. Kurtz S. K. and Perry T. T. (1968). A powder technique for the evaluation of nonlinear optical materials. *J. Appl. Phys.* **39**:3798–3813. DOI:10.1063/1.1656857
45. Clark S. J. and Segall M. D. (2005) Pickard CJ *et al.* First principles methods using CASTEP. *Z.Kristallogr.* **220**:567–570. DOI:10.1524/zkri.220.5.567.65075
46. Kohn W. (1999). Nobel lecture: Electronic structure of matter---wave functions and density functionals. *Rev. Mod. Phys.* **71**:1253–1266. DOI:10.1103/RevModPhys.71.1253
47. Perdew J. P. and Zunger A. (1981). Self-interaction correction to density-functional approximations for many-electron systems. *Phys. Rev. B* **23**:5048–5079. DOI:10.1103/PhysRevB.23.5048
48. Rappe A.M., Rabe K. M., Kaxiras E., et al. (1990) Optimized pseudopotentials. *Phys. Rev. B* **41**:1227–1230. DOI:10.1103/PhysRevB.41.1227
49. Monkhorst H. J. and Pack J. D. (1976). Special points for brillouin-zone integrations. *Phys. Rev. B.* **13**:5188–5192. DOI:10.1103/PhysRevB.13.5188
50. Frisch M. J., Trucks G., Schlegel H. B., et al. (2009). Gaussian 09 Revision A.1. Gaussian Inc.
51. Stephens P. J., Devlin F. J., Chabalowski C. F., et al. (1994). Ab Initio calculation of vibrational absorption and circular dichroism spectra using density functional force fields. *J. Phys. Chem.* **98**:11623–11627. DOI:10.1021/j100096a001
52. Hehre W. J., Ditchfield R. and Pople J. A. (1972). Self—consistent molecular orbital methods. XII. Further extensions of Gaussian—Type basis sets for use in molecular orbital studies of organic molecules. *J. Chem. Phys.* **56**:2257–2261. DOI:10.1063/1.1677527
53. Etter M. C. (1991). Hydrogen bonds as design elements in organic chemistry. *J. Phys. Chem.* **95**:4601–4610. DOI:10.1021/j100165a007
54. Perdew J. P., Burke K., Ernzerhof M. Perdew, et al. (1998). Perdew, burke, and ernzerhof reply. *Phys. Rev. Lett.* **80**:891–891. DOI:10.1103/PhysRevLett.80.891
55. Perdew J. P. and Wang Y. (1997). Erratum: Pair-distribution function and its coupling-constant average for the spin-polarized electron gas. *Phys. Rev. B* **56**:7018–7018. DOI:10.1103/PhysRevB.56.7018
56. Perdew J. P., Burke K. and Ernzerhof M. (1996). Generalized gradient approximation made simple. *Phys. Rev. Lett.* **77**:3865–3868. DOI:10.1103/PhysRevLett.77.3865
57. Perdew J. P. and Wang Y. (1992). Accurate and simple analytic representation of the electron-gas correlation energy. *Phys. Rev. B* **45**:13244–13249. DOI:10.1103/PhysRevB.45.13244
58. Lei B. H., Pan S., Yang Z., et al. (2020). Second harmonic generation susceptibilities from symmetry adapted wannier functions. *Phys. Rev. Lett.* **125**:187402. DOI:10.1103/PhysRevLett.125.187402
59. Lin Z., Wang Z., Chen C., et al. (2003). Mechanism for linear and nonlinear optical effects in crystals of the $Sr_2Be_2B_2O_7$ family. *J. Appl. Phys.* **93**:9717–9723. DOI:10.1063/1.1577816

FUNDING AND ACKNOWLEDGMENTS

This work was financially supported by the Tianshan Talent Training Program (2023TSYCLJ0018, 2024TSYCLJ0038), Key Research and Development Program of Xinjiang (2022B01023-3), Strategic Priority Research Program of the Chinese Academy of Sciences (XDB0880000), and National Natural Science Foundation of China (22335007, 22361132544). The funders had no role in study design, data collection and analysis, decision to publish, or preparation of the manuscript.

AUTHOR CONTRIBUTIONS

J. H. and S.P. conceived and directed the project. G.X. conducted the synthesis and characterization. G.X. and X.B. contributed to the theory calculations. G.X. wrote the manuscript. J. H., S.P., Z.Y., and X.H. contributed to the interpretation and revised the manuscript. All authors contributed to the manuscript and approved the final version.

DECLARATION OF INTERESTS

The authors declare that they have no known competing financial interests or personal relationships that could have appeared to influence the work reported in this paper.

DATA AND CODE AVAILABILITY

Data are available from the corresponding authors upon reasonable request.

SUPPLEMENTAL INFORMATION

It can be found online at https://doi.org/10.59717/j.xinn-mater.2026.100218.

LEAD CONTACT WEBSITE

https://xjipc.cas.cn/rcdw/jcqnnew/200908/t20090812_2380411.html